Morphology of ultrathin lithium fluoride deposited on Ag(100): Dendrites versus islands

V. Romankov and J. Dreiser [*]

Swiss Light Source, Paul Scherrer Institut, CH-5232 Villigen PSI, Switzerland

We have investigated lithium fluoride (LiF) in the monolayer range deposited by thermal sublimation onto the (100) surface of a silver single crystal in ultrahigh vacuum. Our study combines scanning tunneling microscopy, low-energy electron diffraction, and polarized x-ray absorption spectroscopy. The results reveal that LiF grows epitaxially on Ag(100), with a morphology strongly depending on the growth temperature: at room temperature, dendritic patterns are formed with branches along the [011] and [0$\bar{1}$1] directions, exhibiting the same lattice orientation as the substrate. Conversely, at a substrate temperature of 500 K LiF forms square islands exhibiting a moiré pattern, with the islands' borders oriented along the [001] and [010] directions. While the lattice constant of the surface deposited samples is close to the one of bulk fcc LiF, the appearance of a strong x-ray linear dichroism for dendritic LiF points to a tetragonal distortion arising from the LiF-substrate interaction. The less prominent dichroism and the presence of the moiré pattern on the square islands both suggest the relaxation of the LiF grown on the hot Ag substrate.

I. INTRODUCTION

The understanding of the growth of insulating thin films of alkali halides [1–6] and metal oxides [7–9] has motivated fundamental and applied research on this topic in the past decades. In recent years, there has been renewed interest in these materials as they are employed in a large variety of applications such as spin valves [10–12], organic electroluminescent devices [13–15], gas sensors [16], solar cells [17], as well as decoupling layers for single-molecule magnets [18], magnetic atoms [19], and other molecules on surfaces [20].

Among the alkali halides, lithium fluoride (LiF) has the smallest lattice parameter [$a_{LiF} = 0.402(1)$ nm] [21,22] and the largest band gap ($E_g = 13.6$ eV) [23]. It has been previously reported [22,24–27] that, depending on the substrate and the growth temperature, the morphology of LiF deposits can differ strongly from the one of similar alkali halides such as sodium chloride [28–30] and potassium chloride [31], as well as metal oxides like magnesium oxide [32,33]. As pointed out by Farías *et al.* [34], the growth of LiF is not a trivial matter, since it also differs strongly from that of metal on metal growth by forming fractals on both sides of the step edges of Ag(111) at 77 K.

The goal of the present study is to understand the effect of the temperature on the growth and morphology of LiF deposited on the prototypical metal Ag(100) surface and to observe the effect of the substrate symmetry by comparing to the results of Refs. [25,34]. To this end, we have investigated samples with varying thickness in the monolayer regime prepared at different growth temperatures. Scanning tunneling microscopy (STM) reveals the topography, and low-energy electron diffraction (LEED) reveals the structural order in the

ultrathin LiF layers. X-ray absorption spectroscopy at the fluorine K edge yields information about the nearest environment of the fluorine atoms.

II. EXPERIMENT

All experiments were performed at the X-Treme beamline at the Swiss Light Source synchrotron [35]. The samples were prepared and studied under ultrahigh-vacuum conditions, with a base pressure of 3×10^{-10} mbar and without intermediate exposure to air. Polycrystalline LiF powder of 99.99% purity (Sigma-Aldrich) was sublimed from a high-temperature effusion cell after thorough outgassing. A quartz crystal microbalance (QCMB) was used to determine the sublimation rate proportional to the QCMB's frequency shift. The sublimation was performed at temperatures of 975–995 K, which were chosen to keep the sublimation rate the same ($\sim$0.7 Hz/min) for all the samples. We assume the evaporated particle distribution to be the same as reported in literature, mainly composed of monomers (Li$^+$F$^-$) and dimers (Li$_2$$^+F_2$$^-$) [36]. More details can be found in the Supplemental Material [37].

The depositions were performed onto the freshly sputter-annealed (100) surface of a Ag single crystal. Two different growth temperatures were employed to prepare two different sets of samples. The first set was prepared with the Ag crystal at room temperature, while for the second set the substrate was kept at about 500 K. At both substrate temperatures, the samples were prepared in two different ways: first, as a single-shot evaporation and second by adding material on the same sample with consecutive depositions. No notable structural or electronic difference between the two procedures was clearly detected. We define a monolayer (ML) of LiF as the equivalent amount of material present in a close-packed single layer with monoatomic thickness.

_____
[*]jan.dreiser@psi.ch

Linearly polarized x-ray absorption spectra were recorded in the proximity of the fluorine K edge, without breaking the vacuum during the sample transfer. The normal of the Ag(100) plane was oriented at 60° from the propagation vector of the incoming photon beam. X-ray absorption is defined as the sum of the linearly polarized spectra $\mu_{XAS} = \mu_h + \mu_v$ and the x-ray linear dichroism (XLD) as the difference $\mu_{XLD} = \mu_v - \mu_h$. The spectra were normalized to the intensity of the main x-ray absorption spectroscopy (XAS) peak at ∼690.5 eV after subtracting the baseline. LiF polycrystalline powder was used as a reference of bulk LiF. The acquisition was carried out in the total electron yield mode, and the measurements were performed using a defocused spot size of ∼0.5 mm^2 to prevent radiation damage.

The surface characterization was performed *in situ* at room temperature by using a commercial scanning tunneling microscope (Omicron VT-STM) with a tungsten tip. STM images were acquired in constant current mode with the current set-point I_s ranging from 1 to 10 pA. The bias voltage V_b was applied to the sample, while the tip was grounded.

The LEED patterns were recorded at specific electron-beam energies $E_{beam} = 60$, 112, and 140 eV with a fixed Wehnelt potential. The contrast of the images was scaled such that black (white) represents the minimum (maximum) intensity for each LEED pattern, respectively. In the main text we report only the 60-eV patterns as they are representative of the surface structure of the samples. All other LEED patterns are shown in the Supplemental Material [37]. No clear change of the LEED patterns over time was observed under the exposure to the electron beam. Similarly, no time-dependent changes were detected during the x-ray spectroscopy experiments.

The microscopic model shown in Fig. 4 was obtained using the MERCURY 4.0 software [38].

III. RESULTS

A. STM and LEED

1. Dendrites

In Fig. 1 representative STM images of LiF deposited on Ag(100) at room temperature are shown, together with the corresponding LEED patterns obtained at an electron energy of 60 eV. The images in Figs. 1(a)–1(d) reveal that LiF assembles into dendrites, nucleating both on the terraces and at the step edges (see also Supplemental Material [37]). The extension of the main and the secondary branches is strongly anisotropic and follows two axes oriented at an angle of 90° with respect to each other, exhibiting a weak in-plane mosaicity of up to 5°. The comparison of the dendrites in Fig. 1 with atomically resolved images of the substrate (Supplemental Material [37]) identifies these axes to be the [011] and [0$\bar{1}$1] directions of the substrate. The length of the main branches changes with the amount of deposited material up to a maximum extension of ∼250 nm for the thickest sample reported in Fig. 1(d). At low bias voltages such as $V_b = +1$ V ($I_s = 5$ pA), the dendrites show an inverted contrast as visible in Figs. 1(a) and 1(b), with apparent depths of up to −1 nm (see Supplemental Material [37]). A line profile shown as a blue curve in Fig. 1(e) displays the first two LiF steps exhibiting an apparent height of −0.25 and −0.5 nm, with respect to
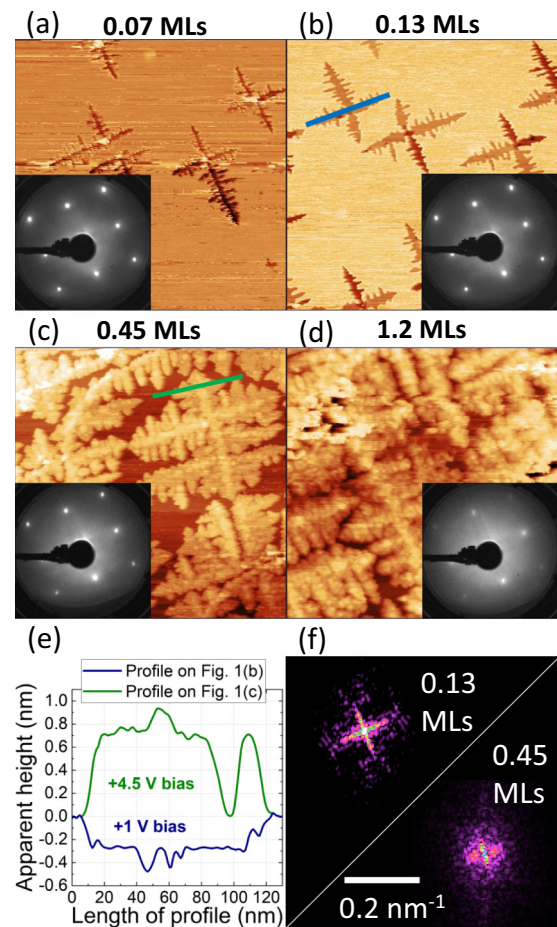

FIG. 1. Constant-current 400×400-nm^2 STM images of LiF/Ag(100) at different coverages deposited at room temperature, and corresponding LEED patterns at $E_{beam} = 60$ eV. (a), (b) $V_b = +1$ V, $I_s = 5$ pA; (c) $V_b = +4.5$ V, $I_s = 1$ pA; (d) $V_b = +4.2$ V, $I_s = 1$ pA. (e) Line profiles extracted along the blue and green lines in panels (b) and (c), respectively; (f) Fourier transforms extracted from panels (b) and (c).

the level of the substrate. Some STM images such as the one reported in Fig. 1(a) display a sharp feature at the center node, which could be attributed to impurities or defects acting as nucleation centers.

For bias voltages above +4.2 V [Figs. 1(c) and 1(d)], the dendrites exhibit a contrast reversal, with protrusions up to an apparent height of 1 nm. This contrast inversion can be understood by the injection of the current into the LiF conduction band, which is possible at a large enough bias voltage, at which the LiF conduction band edge becomes aligned with the Fermi level of the STM metal tip. A proper dI/dV spectroscopic study could not be performed because of thermal and other drifts of both the tip and the sample. However, no further contrast changes were observed in the range -6 V $< V_b < +6$ V, supporting the aforementioned contrast reversal mechanism in this large band-gap material.

Referring to the images with a positive contrast, the dendrites prefer a vertical growth rather than a full closure of the substrate, with an apparent height of ∼0.7 nm for the first step and ∼0.25 nm for the second one. A spatially inhomogeneous

vertical growth of the dendrites is observed in the line profiles such as the one extracted along the green line in Fig. 1(c) and reported by the green curve in Fig. 1(e).

The length and the lateral size of the secondary branches vary with the amount of material. This becomes visible in the two Fourier transforms (FT) [cf. Fig. 1(f)] obtained from the STM images shown in Figs. 1(b) and 1(c). The FT of the 0.13-ML sample exhibits a well-defined crosslike shape given by the main and the secondary branches. Upon increasing the amount of material to 0.45 MLs, both the smearing of the contours and the inhomogeneous vertical growth increase, which is reflected in the less pronounced Fourier pattern in Fig. 1(f).

LEED patterns reported in Figs. 1(a)–1(d) do not show any additional diffraction points other than the ones of Ag(100). In conclusion, LiF exhibits the same fourfold symmetry of its atomic structure and the same lattice constant, as the one of the substrate, with an error corresponding to the width of the spots. Upon increasing the amount of deposited material, the broadening of the diffraction spots and the background intensity increase, while the intensity of the spots exhibits a progressive fading. Note that for larger coverages of LiF the (1,1) spots, which are at the corners of the diffraction pattern, show considerably less intensities with respect to the (1,0) points.

2. Square islands

The STM images reported in Figs. 2(a)–2(d) show that LiF assembles in a strikingly different manner on a hot substrate, forming compact square islands with increasing lateral sizes of up to ∼200 nm for the largest amount of deposited material. The images collected at a current setpoint of 10 pA and a bias of +4.5 V exhibit a positive contrast, that is, the islands appear as protrusions with a positive apparent height. Similar to the case of dendritic LiF a contrast inversion is observed for lower bias voltages (see Supplemental Material [37]).

Layer-by-layer growth is not observed, as the second and subsequent layers nucleate before reaching full closure of the substrate surface [Figs. 2(c) and 2(d)]. The apparent height of the first layer with respect to the substrate level is ∼0.4 nm, while successive layers have a height of ∼0.25 nm, up to a maximum detected thickness of ∼4 nm in Fig. 2(d). The borders of the square islands are aligned with the [001] and [010] directions of the substrate, with a weak mosaicity of a few degrees.

On the LiF islands, a modulation of the local density of states (LDOS) is observed to form a square lattice oriented along the [011] and [0$\bar{1}$1] directions of the substrate, that is, at 45° with respect to the edges of the LiF islands. As an example, a line profile is extracted from Fig. 2(b) and reported in Fig. 2(e), showing two LiF step edges and the modulation. The analysis of the line profiles reveals that the primitive cell of the modulation has a lattice parameter in the range of 13.9–18.6 nm. This can be understood by the small in-plane mosaicity of the islands, which will be addressed further below.

Figure 2(f) shows a 120 × 120-nm^2 zoom extracted from Fig. 2(b), where the primitive cell of the modulation can be clearly observed. A Fourier transform of this image is also reported, showing a sharp cross in the middle, oriented along
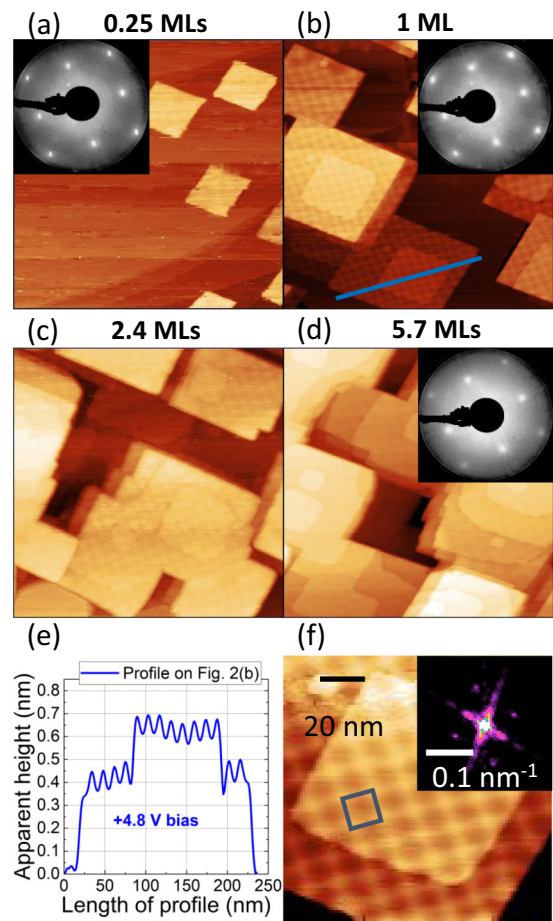

FIG. 2. Constant-current 400 × 400-nm^2 STM images of LiF/Ag(100) at different coverages deposited at 500 K, and corresponding LEED patterns at $E_{beam} = 60$ eV. (a) $V_b = +5.8$ V, $I_s = 10$ pA; (b)–(d) $V_b = +4.8$ V, $I_s = 10$ pA. (e) Line profile extracted along the blue line in panel (b); (f) 120 × 120-nm^2 zoom of a square LiF island, extracted from panel (b), and its Fourier transform. The gray square has a size of 13.9 nm and highlights the primitive cell of the modulation pattern.

the [010] and [001] directions and originating from the square symmetry of the islands. On the same pattern, four spots rotated by 45° (±5°) with respect to the cross are oriented along the [011] and [0$\bar{1}$1] directions, originating from the square lattice of the modulation.

The LEED patterns in Figs. 2(a)–2(d) exhibit the same diffraction spots as the Ag(100) surface (see Supplemental Material [37]). The intensity of the spots decreases gradually with the amount of deposited LiF, and an increasingly diffuse halo develops around the spots. Again, for the largest sample, a net difference in brightness between the (1,0) and (1,1) spots was detected. No additional diffraction spots deviating from the Ag(100) pattern were found.

B. X-ray absorption spectroscopy

X-ray absorption spectroscopy at the fluorine K edge was performed on the LiF/Ag(100) samples using linearly polarized x-rays, which allowed us to address in-plane fluorine orbitals with vertical polarization (μ_v) and mostly

out-of-plane orbitals with horizontal polarization (μ_{h}). Figure 3(a) shows selected absorption spectra of LiF/Ag(100) grown at 300 and 500 K.

While the spectra obtained on the square islands are virtually identical to the ones of bulk LiF, the spectra obtained on the dendrites exhibit a slight smearing of the features. For better visibility, Fig. 3(b) shows the difference $\delta_{\mathrm{XAS}} = \mu_{\mathrm{bulk}} - \mu_{\mathrm{surf}}$ between each spectrum reported in Fig. 3(a) and the one of the LiF powder. The lowest coverages of LiF exhibit a less-defined shape of the XAS peaks, while the spectra approach the shape of bulk LiF upon increasing the thickness. This effect is minimal for LiF grown on the hot substrate, while it is strong in the case of room-temperature growth. The major difference appears at a photon energy of $\sim$690.5 eV, which is caused by the shift of the peak maximum toward lower energies by 0.4 eV for submonolayer amounts of LiF.

Figure 3(c) reports the normalized linear dichroism. The analysis of the data reveals that the XLD intensity of the dendrites is larger by a factor of $\sim$4 as compared to the LiF islands. Furthermore, for both dendrites and islands the XLD intensity decreases with increasing average thickness. The samples with an estimated thickness of 2.4 and 5.8 MLs grown on hot Ag display a very similar XLD value of $\sim$0.7% at the peak maximum (694.4 eV), suggesting that a saturation of the XLD has been reached.

The comparison of the fluorine K-edge XAS of LiF to the ones of copper fluoride (CuF_2) and polytetrafluoroethylene (PTFE), as plotted in Fig. S7(b) of the Supplemental Material [37], reveals a unique shape, confirming that the deposited material virtually has the same stoichiometry and structure of bulk LiF.

IV. DISCUSSION

Our results clearly show that the morphology of LiF deposited on Ag(100) crucially depends on the temperature of the substrate during the deposition. The qualitative difference between dendritic and island growth is strong and in contrast to the typical square-shaped island morphology of sodium chloride [28–30] and magnesium oxide on metallic substrates [33] obtained at comparable growth temperatures.

The fractal growth of LiF, which has been reported on Ag(111) at liquid nitrogen temperature [25,34], and the present results indicate that the substrate and its surface symmetry play an important role on the anisotropic growth of LiF. The formation of dendrites can be understood by the anisotropic diffusion which is preferred along the [011] and [0$\bar{1}$1] directions of the substrate, that is, along the rows of the nearest-neighbor surface Ag atoms. Predominantly, Li^+–F^- monomers and to a lesser extent $Li_2^+F_2^-$ dimers are generated during thermal sublimation of LiF [36]. Accordingly, it is assumed that the smallest stable diffusing units correspond to this vapor phase distribution [25]. It is likely that the larger F^- ion plays a dominant role in the diffusion process of monomers and dimers along the shortest Ag-Ag distance, or rather the potential valleys formed between Ag atoms along the [011] and [0$\bar{1}$1] directions, as shown in Fig. 4(a). Surface defects or impurities act as nucleation centers, where diffusing LiF units agglomerate, as already observed on the Ag(111)
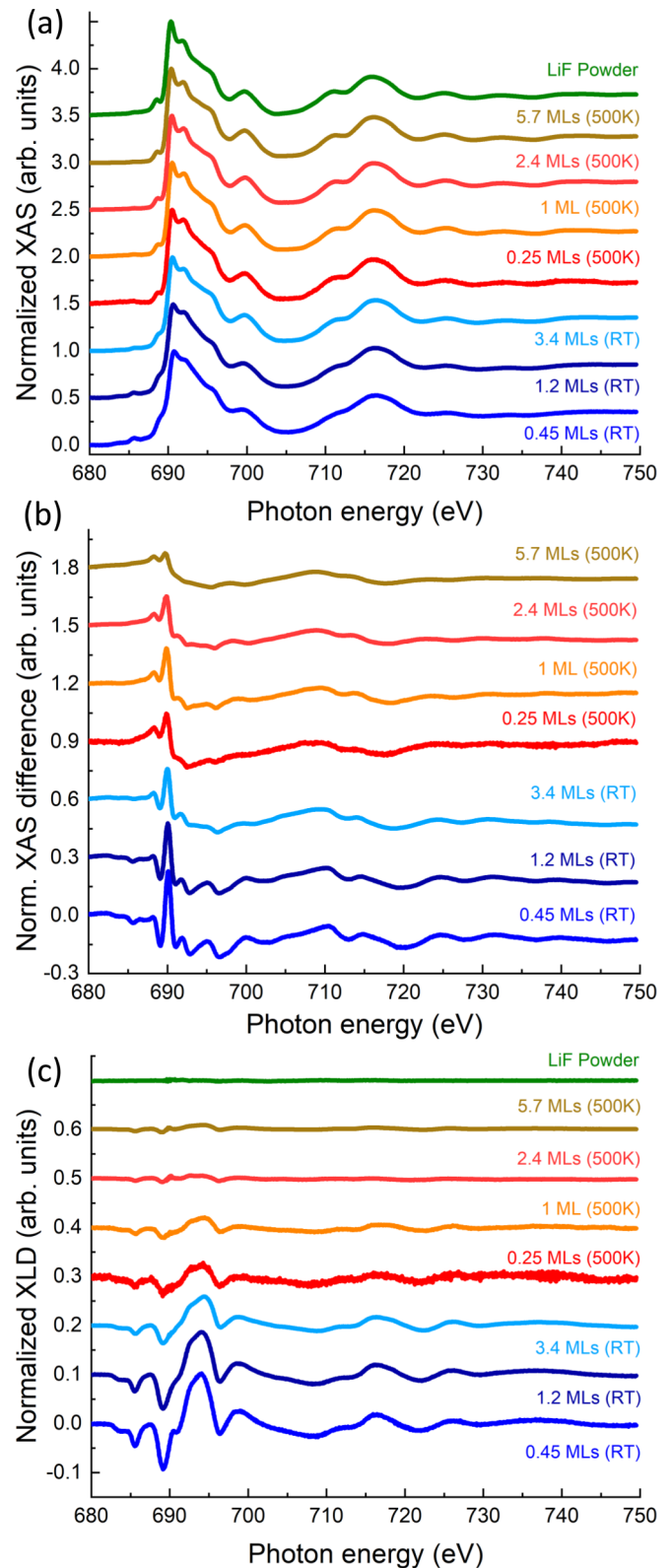

FIG. 3. (a) Normalized x-ray absorption spectra recorded on different coverages of LiF/Ag(100) at the fluorine K edge as indicated in the plots. (b) Differences between the normalized absorption spectra of LiF powder and the XAS of LiF grown on Ag(100). (c) X-ray linear dichroism ($\mu_{\mathrm{v}} - \mu_{\mathrm{h}}$). The spectra are vertically offset for better visibility.
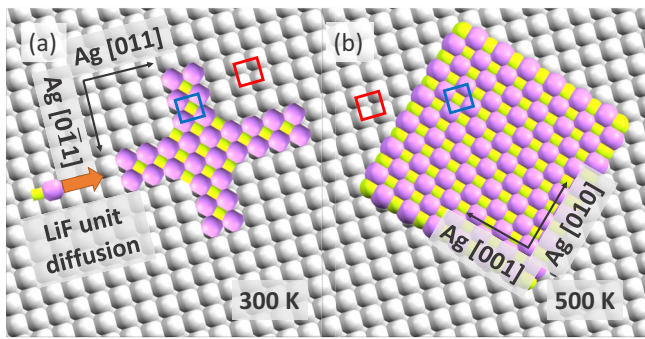
FIG. 4. Microscopic model of (a) the dendrites and (b) the square islands of LiF/Ag(100). The LiF lattice has the same orientation as the one of the substrate in both cases, with a partial relaxation of LiF in (b) (not visible). The relevant crystallographic directions are indicated along with the primitive unit cells of Ag (red) and LiF (blue). The orange arrow in (a) indicates the preferred direction of the surface diffusion of LiF units at room temperature. Color code: gray, Ag; purple, F^-; green, Li^+ [38].

surface [34]. The in-plane growth is then limited mostly to the aforementioned directions, as corner and step diffusion would require the LiF units to overcome a certain energy barrier, which is higher than its thermal energy at room temperature. The formation of a few large dendrites instead of many small ones is a hint of surface diffusion across a large spatial extent even for the substrate held at room temperature.

The dendrites and islands both grow epitaxially. For very low coverages of LiF, the contribution of the adsorbate to the LEED pattern is indistinguishable from the one of the bare Ag(100) surface. Nevertheless, the absence of new diffraction spots across the whole coverage series regardless of the growth temperature indicates that the LiF lattice is always aligned with the one of the substrate. Indeed, the LEED patterns exhibit the fourfold symmetry reported for a bulk LiF(100) surface [39] with the diffraction spots matching the ones of the silver substrate. This behavior is expected because of the small lattice mismatch between Ag ($a_{Ag} = 0.4086$ nm) [40] and LiF [$a_{LiF} = 0.402(1)$ nm] [21,22], unlike, e.g., the case of NaCl/Ag(100), where a large lattice mismatch typically causes an incommensurate growth [41]. For LEED patterns taken at 60 eV (Fig. 1) and 112 eV (Supplemental Material [37]) the intensities of the (1,1) spots are lower with respect to the (1,0) spots. A similar pattern has been observed on LiF/Si(100) [26] after 1-min annealing at about 600 K, as well as at specific electron-beam energies of compounds with a unit cell composed of two atomic species, like NaCl [42] and MgO [43]. The LEED patterns acquired at 140 eV and reported in the Supplemental Material [37] show the opposite trend, with the (1,1) spot intensities stronger than that of (1,0) spots, similar to the trend of the reported LEED intensities of bulk LiF [39].

Upon increasing the amount of LiF, the dendrites exhibit a progressive fading and broadening of the LEED diffraction spots, suggesting a reduction of the local ordering because of, e.g., defects. It is reasonable to assume that the electrostatic interaction between the Li^+ and F^- ions limits the diffusion of LiF units on the dendrites. This causes an inhomogeneous

vertical growth of the dendrites, which is visible in the STM line profiles, such as the one in Fig. 1(e). The small in-plane mosaicity observed in the STM images and a relaxation of the LiF lattice parameter with the dendrite thickness could also be affecting the shape of the diffraction spots. The latter hypothesis is supported by the fact that thicker samples show a reduction of the XLD intensity by up to a factor of 1.7 when increasing the LiF thickness from 0.45 to 3.4 MLs (Fig. 3). Possibly, the charging of the insulating LiF under the electron beam of the LEED instrument could also contribute to the broadening of the spots.

The measured absorption spectra in the present work are in excellent agreement with the experiment data found in the literature [44,45], as well as with the reported simulations of the fluorine K edge of bulk LiF [46,47]. The comparison of the fluorine K-edge spectra of the monolayer deposit with the ones of polycrystalline powder of LiF, CuF_2, and PTFE, as shown in the Supplemental Material [37], reveals that LiF maintains the general electronic bulk properties and stoichiometry in the (sub)monolayer and few-layer ranges. The previously mentioned linear dichroism, which we observe on all the surface-deposited LiF samples, can be attributed to the symmetry breaking of the $2p$ orbitals, which happens for two main reasons: First, at the LiF-vacuum and the LiF-Ag interfaces the otherwise octahedral symmetry of the local environment of the fluoride ions is broken. Second, the tetragonal distortion of the lattice caused by lateral strain, which LiF undergoes to match the lattice constant of the substrate, also leads to a departure from octahedral symmetry. The latter effect is expected to be strongest close to the LiF-Ag interface. The difference in XLD intensity by a factor of ∼4 between the dendrites and the islands can be understood by a different degree of strain in the LiF. The strong reduction of XLD intensities for thicker samples suggests that a relaxation of the lattice parameter with increasing LiF thickness occurs but the relative interfacial contributions to the XLD are also expected to decrease with increasing LiF thickness.

At a growth temperature of 500 K LiF forms compact square islands, which is explained by a faster and more isotropic diffusion of LiF units on both the Ag and LiF surfaces. The islands deviate from a perfect square shape when more material is deposited; however, the borders are all aligned along the [010] and [001] directions of the substrate within a few degrees, as seen in Fig. 4(b). As mentioned previously, such a morphology has been reported for other alkali halides deposited on metal substrates, which places the observed LiF islands in line with the previously reported cases [28–33].

Moreover, the apparent step height of the first layer of dendritic LiF amounts to 0.7 nm, which corresponds to about the height of the second layer of the square LiF. This suggests that the dendrites grow with an initial double layer to avoid polar edges along the [011] and [0$\bar{1}$1] directions. The observation of square-shaped relaxed islands at a growth temperature of 500 K as well as the nucleation of the subsequent layers before completion of the first layer suggest the possibility of a Volmer-Weber type of growth. Yet, this morphology would also be consistent with a kinetic roughening effect, where LiF units cannot descend quickly enough from an island before nucleating the next layer.

The presence of a modulation pattern in the STM images recorded on the LiF islands is ascribed to the moiré effect originating from the relaxed LiF overlayer on the substrate. Indeed, for a fully relaxed overlayer without rotation relative to the Ag(100) surface, a moiré pattern with a lattice parameter of 24.9 nm would be expected. We find varying moiré lattice parameters in the range of 18.7–26.4 nm, in good agreement with the expected one. Larger values can be attributed to a partial tensile strain of the LiF lattice, while smaller values to small lattice rotations of LiF with respect to the Ag lattice. The latter assumption is in line with the observed weak in-plane mosaicity, also because lattice rotations even below 1° affect strongly the lattice parameter of the moiré. A similar moiré lattice has been reported for NaCl/Ag(100), where the LDOS modulation was explained in terms of the modulation of the local work function through a shift of the image-state potential [30,48]. It is reasonable to assume that the same mechanism is at the basis of the LDOS modulation reported in the present work, too, given the same substrate and the similarities of the two alkali halides.

A broadening of the LEED spots with increasing thickness of LiF islands is observed. In principle, the moiré pattern is expected to lead to the appearance of satellite spots in the LEED pattern. Yet, because of the large supercell size of the moiré, the satellites appear within the instrumental width of the main spots, thus contributing to the broadening of the diffraction spots. Similarly, the mosaicity appears like a small angular smearing. Furthermore, the gradual relaxation of the LiF lattice parameter deduced from the XLD upon increasing the island's thickness, contributes to the spot broadening.

V. CONCLUSIONS

In the present work we have determined the growth type and the morphology of thermally deposited lithium fluoride in the monolayer range on the Ag(100) surface. LiF exhibits epitaxial growth with the same lattice orientation as the one of the substrate. A vertical growth is preferred over the layer-by-layer growth, while the morphology strongly depends on the growth temperature. In particular, at room temperature the anisotropic diffusion leads to the assembly of LiF into dendrites oriented along the [011] and [0$\bar{1}$1] directions of the Ag(100) substrate.

When the deposition occurs on the hot substrate, LiF forms compact square islands, with edges along the nonpolar [010] and [001] directions. The mismatch of the lattice constants between the overlayer and the substrate gives rise to a moiré pattern detected in the STM images. The XLD results reveal that the square islands are less strained compared to the dendrites. Our results demonstrate that LiF/Ag(100) is an interesting model system, in which a strong qualitative change of the morphology can be controlled by the growth temperature.

[1] M. H. Yang and C. P. Flynn, Growth of Alkali Halides from Molecular Beams: Global Growth Characteristics, Phys. Rev. Lett. **62**, 2476 (1989).

[2] M. Kiguchi, S. Entani, K. Saiki, H. Inoue, and A. Koma, Two types of epitaxial orientations for the growth of alkali halide on fcc metal substrates, Phys. Rev. B **66**, 155424 (2002).

[3] J. Baker and P.-A. Lindgård, Heteroepitaxial strain in alkali halide thin films: KCl on NaCl, Phys. Rev. B **60**, 16941 (1999).

[4] A. Riemann, S. Fölsch, and K. H. Rieder, Epitaxial growth of alkali halides on stepped metal surfaces, Phys. Rev. B **72**, 125423 (2005).

[5] C. Loppacher, U. Zerweck, and L. M. Eng, Kelvin probe force microscopy of alkali chloride thin films on Au(111), Nanotechnology **15**, S9 (2004).

[6] S. Prada, U. Martinez, and G. Pacchioni, Work function changes induced by deposition of ultrathin dielectric films on metals: A theoretical analysis, Phys. Rev. B **78**, 235423 (2008).

[7] H.-J. Freund, H. Kuhlenbeck, and V. Staemmler, Oxide surfaces, Rep. Prog. Phys. **59**, 283 (1996).

[8] S. A. Chambers, Epitaxial growth and properties of thin film oxides, Surf. Sci. Rep. **39**, 105 (2000).

[9] S. Schintke and W.-D. Schneider, Insulators at the ultrathin limit: Electronic structure studied by scanning tunnelling microscopy and scanning tunnelling spectroscopy, J. Phys.: Condens. Matter **16**, R49 (2004).

[10] Y. M. Lee, J. Hayakawa, S. Ikeda, F. Matsukura, and H. Ohno, Effect of electrode composition on the tunnel magnetoresistance of pseudo-spin-valve magnetic tunnel junction with a MgO tunnel barrier, Appl. Phys. Lett. **90**, 212507 (2007).

[11] A. J. Drew, J. Hoppler, L. Schulz, F. L. Pratt, P. Desai, P. Shakya, T. Kreouzis, W. P. Gillin, A. Suter, N. A. Morley, V. K. Malik, A. Dubroka, K. W. Kim, H. Bouyanfif, F. Bourqui, C. Bernhard, R. Scheuermann, G. J. Nieuwenhuys, T. Prokscha, and E. Morenzoni, Direct measurement of the electronic spin diffusion length in a fully functional organic spin valve by low-energy muon spin rotation, Nat. Mater. **8**, 109 (2009).

[12] J.-Y. Choi, D. Lee, J.-U. Baek, and J.-G. Park, Double MgO-based perpendicular magnetic-tunnel-junction spin-valve structure with a top Co$_2$Fe$_6$B$_2$ free layer using a single SyAF [Co/Pt]$_n$ Layer, Sci. Rep. **8**, 2139 (2018).

[13] L. S. Hung, C. W. Tang, and M. G. Mason, Enhanced electron injection in organic electroluminescence devices using an Al/LiF electrode, Appl. Phys. Lett. **70**, 152 (1997).

[14] H. Heil, J. Steiger, S. Karg, M. Gastel, H. Ortner, H. Von Seggern, and M. Stößel, Mechanisms of injection enhancement in organic light-emitting diodes through an Al/LiF Electrode, J. Appl. Phys. **89**, 420 (2001).

[15] T. M. Brown, R. H. Friend, I. S. Millard, D. J. Lacey, T. Butler, J. H. Burroughes, and F. Cacialli, Electronic line-up in light-emitting diodes with alkali-halide/metal cathodes, J. Appl. Phys. **93**, 6159 (2003).

[16] A. Dey, Semiconductor metal oxide gas sensors: A review, Mater. Sci. Eng., B **229**, 206 (2018).

[17] J. Bullock, P. Zheng, Q. Jeangros, M. Tosun, M. Hettick, C. M. Sutter-Fella, Y. Wan, T. Allen, D. Yan, D. Macdonald, S. De Wolf, A. Hessler-Wyser, A. Cuevas, and A. Javey, Lithium fluoride based electron contacts for high efficiency n-type crystalline silicon solar cells, Adv. Energy Mater. **6**, 1 (2016).

[18] C. Wäckerlin, F. Donati, A. Singha, R. Baltic, S. Rusponi, K. Diller, F. Patthey, M. Pivetta, Y. Lan, S. Klyatskaya, M. Ruben, H. Brune, and J. Dreiser, Giant hysteresis of single-molecule magnets adsorbed on a nonmagnetic insulator, Adv. Mater. **28**, 5195 (2016).

[19] F. Donati, S. Rusponi, S. Stepanow, C. Wäckerlin, A. Singha, L. Persichetti, R. Baltic, K. Diller, F. Patthey, E. Fernandes, J. Dreiser, Ž. Šljivančanin, K. Kummer, C. Nistor, P. Gambardella, and H. Brune, Magnetic remanence in single atoms, Science **352**, 318 (2016).

[20] J. Repp, G. Meyer, S. M. Stojković, A. Gourdon, and C. Joachim, Molecules on Insulating Films: Scanning-Tunneling Microscopy Imaging of Individual Molecular Orbitals, Phys. Rev. Lett. **94**, 026803 (2005).

[21] J. Thewlis, Unit-cell dimensions of lithium fluoride made from Li^6 and Li^7, Acta Crystallogr. **8**, 36 (1955).

[22] R. M. Montereali, G. Baldacchini, S. Martelli, and L. C. S. Do Carmo, LiF films: Production and characterization, Thin Solid Films **196**, 75 (1991).

[23] D. M. Roessler and W. C. Walker, Electronic spectrum of crystalline lithium fluoride, J. Phys. Chem. Solids **28**, 1507 (1967).

[24] D. A. Lapiano-Smith, E. A. Eklund, F. J. Himpsel, and L. J. Terminello, Epitaxy of LiF on Ge(100), Appl. Phys. Lett. **59**, 2174 (1991).

[25] K.-F. Braun, D. Farias, S. Fölsch, and K.-H. Rieder, Fractal growth of LiF on Ag(111) studied by low-temperature STM, Surf. Sci. **454-456**, 750 (2000).

[26] F. Gołek and P. Mazur, LiF thin layers on Si(100) studied by ESD, LEED, AES, and AFM, Surf. Sci. **541**, 173 (2003).

[27] H. Kim and A. H. King, Grain growth and texture development in lithium fluoride thin films, J. Mater. Res. **23**, 452 (2008).

[28] R. Bennewitz, V. Barwich, M. Bammerlin, C. Loppacher, M. Guggisberg, A. Baratoff, E. Meyer, and H. J. Güntherodt, Ultrathin films of NaCl on Cu(111): A LEED and dynamic force microscopy study, Surf. Sci. **438**, 289 (1999).

[29] W. Hebenstreit, J. Redinger, Z. Horozova, M. Schmid, R. Podloucky, and P. Varga, Atomic resolution by STM on ultrathin films of alkali halides: Experiment and local density calculations, Surf. Sci. **424**, L321 (1999).

[30] M. Pivetta, F. Patthey, M. Stengel, A. Baldereschi, and W.-D. Schneider, Local work function moiré pattern on ultrathin ionic films: NaCl on Ag(100), Phys. Rev. B **72**, 115404 (2005).

[31] M. Müller, J. Ikonomov, and M. Sokolowski, Structure of epitaxial layers of KCl on Ag(100), Surf. Sci. **605**, 1090 (2011).

[32] S. Schintke, S. Messerli, M. Pivetta, F. Patthey, L. Libioulle, M. Stengel, A. De Vita, and W.-D. Schneider, Insulator at the Ultrathin Limit: MgO on Ag(001), Phys. Rev. Lett. **87**, 276801 (2001).

[33] S. Baumann, I. G. Rau, S. Loth, C. P. Lutz, and A. J. Heinrich, Measuring the three-dimensional structure of ultrathin insulating films at the atomic scale, ACS Nano **8**, 1739 (2014).

[34] D. Farías, K. F. Braun, S. Fölsch, G. Meyer, and K. H. Rieder, Observation of a novel nucleation mechanism at step edges: LiF molecules on Ag(111), Surf. Sci. **470**, L93 (2000).

[35] C. Piamonteze, U. Flechsig, S. Rusponi, J. Dreiser, J. Heidler, M. Schmidt, R. Wetter, M. Calvi, T. Schmidt, H. Pruchova, J. Krempasky, C. Quitmann, H. Brune, and F. Nolting, X-treme beamline at SLS: X-ray magnetic circular and linear dichroism at high field and low temperature, J. Synchrotron Radiat. **19**, 661 (2012).

[36] G. M. Rothberg, M. Eisenstadt, and P. Kusch, Free evaporation of alkali halide crystals, J. Chem. Phys. **30**, 517 (1959).

[37] See Supplemental Material at http://link.aps.org/supplemental/10.1103/PhysRevB.104.195401 for more information about the sample preparation and additional STM images, LEED patterns, and x-ray absorption spectra.

[38] C. F. MacRae, I. Sovago, S. J. Cottrell, P. T. A. Galek, P. McCabe, E. Pidcock, M. Platings, G. P. Shields, J. S. Stevens, M. Towler, and P. A. Wood, Mercury 4.0: From visualization to analysis, design and prediction, J. Appl. Crystallogr. **53**, 226 (2020).

[39] J. Vogt and H. Weiss, The structure of KBr(100) and LiF(100) single crystal surfaces: A tensor low energy electron diffraction analysis, Surf. Sci. **501**, 203 (2002).

[40] I. K. Suh, H. Ohta, and Y. Waseda, High-temperature thermal expansion of six metallic elements measured by dilatation method and x-ray diffraction, J. Mater. Sci. **23**, 757 (1988).

[41] E. Le Moal, M. Müller, O. Bauer, and M. Sokolowski, Misfit driven azimuthal orientation of NaCl domains on Ag(100), Surf. Sci. **603**, 2434 (2009).

[42] J. Vogt, Tensor LEED study of the temperature dependent dynamics of the NaCl(100) single crystal surface, Phys. Rev. B **75**, 125423 (2007).

[43] S. Valeri, S. Altieri, A. di Bona, P. Luches, C. Giovanardi, and T. S. Moia, Thickness-dependent strain in epitaxial MgO layers on Ag(001), Surf. Sci. **507-510**, 311 (2002).

[44] E. Hudson, E. Moler, Y. Zheng, S. Kellar, P. Heimann, Z. Hussain, and D. A. Shirley, Near-edge sodium and fluorine k-shell photoabsorption of alkali halides, Phys. Rev. B **49**, 3701 (1994).

[45] K. Hämäläinen, S. Galambosi, J. A. Soininen, E. L. Shirley, J.-P. Rueff, and A. Shukla, Momentum dependence of fluorine k-edge core exciton in lif, Phys. Rev. B **65**, 155111 (2002).

[46] Y. Joly, C. Cavallari, S. A. Guda, and C. J. Sahle, Full-potential simulation of x-ray Raman scattering spectroscopy, J. Chem. Theory Comput. **13**, 2172 (2017).

[47] J. Vinson, J. J. Rehr, J. J. Kas, and E. L. Shirley, Bethe-Salpeter equation calculations of core excitation spectra, Phys. Rev. B **83**, 115106 (2011).

[48] H.-C. Ploigt, C. Brun, M. Pivetta, F. Patthey, and W.-D. Schneider, Local work function changes determined by field emission resonances: NaCl/Ag(100), Phys. Rev. B **76**, 195404 (2007).